



## Short communication

## Modeling of combined capacity fade with thermal effects for a cycled $\text{Li}_x\text{C}_6-\text{Li}_y\text{Mn}_2\text{O}_4$ cell

Jorge Vazquez-Arenas<sup>a,\*</sup>, Michael Fowler<sup>a</sup>, Xiaofeng Mao<sup>b</sup>, Shih-ken Chen<sup>b</sup><sup>a</sup>Chemical Engineering Department, University of Waterloo, 200 University Avenue West, Waterloo, ON, Canada N2L 3G1<sup>b</sup>Electrical & Controls Integration Lab, 30500 Mound Rd, General Motors R&D, Warren, MI 48090, USA

## HIGHLIGHTS

- Modeling of thermal and capacity fade effects for a  $\text{Li}_x\text{C}_6-\text{Li}_y\text{Mn}_2\text{O}_4$  cell.
- Capacity fade effects at anode and cathode were found to be significant during cycling.
- SEI formation operates under steady-state conditions during battery cycling.
- Degradation of the cell is more prominent during the dissolution of  $\text{Li}_y\text{Mn}_2\text{O}_4$  particles.

## ARTICLE INFO

## Article history:

Received 26 January 2012

Received in revised form

25 April 2012

Accepted 29 April 2012

Available online 7 May 2012

## Keywords:

Li-ion battery

Thermal effects

Capacity fade

Modeling

Cycling

## ABSTRACT

Li-ion batteries are the most promising technology for use in electric vehicles in the near future, and as such it is critical to understand their performance at both beginning of life (BOL) and end of life (EOL). In this work different thermal and capacity fade effects (e.g. SEI formation, dissolution of  $\text{Li}_y\text{Mn}_2\text{O}_4$  particles) are modeled to account comprehensively for the behavior of a  $\text{Li}_x\text{C}_6-\text{Li}_y\text{Mn}_2\text{O}_4$  cell. The comparison between baseline and complex models is systematically used to analyze individual contributions and perform a deeper evaluation of the variables affecting the capacity fade with thermal inputs during typical cycle life tests. Some modifications in the original model are proposed to better describe the behavior of the cell and speed up the calculations.

© 2012 Elsevier B.V. All rights reserved.

## 1. Introduction

Interest in modeling dual-lithium insertion cells has gained popularity to tackle industrial demands because of its efficiency in testing Li-ion batteries. Li-ion batteries are the most promising technology for use in electric vehicles in the near future. Within the automotive environment the batteries will experience demanding thermal condition (both high and low temperature), large state of charge swings, and high power draws. All of these harsh operating conditions have the potential to degrade both the power and capacity performance of the cells. Therefore, it is critical to understand their performance at beginning of life (BOL) and end of life (EOL). Modeling is also a powerful method to analyze failure

mechanisms (e.g. capacity fade) and thermal runaway during long cycle life tests [1]. Arora et al. [2] reviewed the capacity loss mechanisms associated with phase changes in the inserted electrode materials, electrolyte decomposition, active material dissolution, passive film formation, etc. Although all these phenomena could be responsible for the capacity fade in batteries; the consumption of lithium at the anode during cell charge [2–4] and cathode dissolution (e.g.  $\text{Li}_y\text{Mn}_2\text{O}_4$  spinels) [4] have been acknowledged as the most dominant effects. In this direction, Spotnitz used modeling to propose that two major processes dominate the capacity loss, namely, impedance growth at both electrodes and loss of active lithium at anode [3]. Christensen and Newman also suggested that the use of cutoff potentials may not prevent undesired parasitic reactions (e.g. Li salt and solvent consumptions at the anode, dissolution of  $\text{Li}_y\text{Mn}_2\text{O}_4$  particles) occurring during overcharge [4]. Ning et al. [5] modeled the capacity fade of Li-ion batteries considering a solvent reduction (EC) reaction occurring during the charging process. This model

\* Corresponding author. Tel.: +1 519 888 4567x31622; fax: +1 519 746 4979.

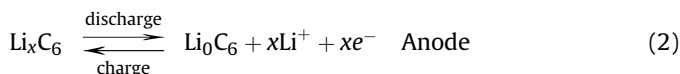
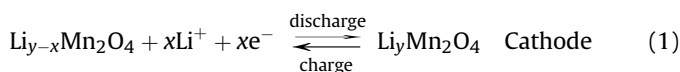
E-mail addresses: [jgvazque@uwaterloo.ca](mailto:jgvazque@uwaterloo.ca), [jorge\\_gva@hotmail.com](mailto:jorge_gva@hotmail.com) (J. Vazquez-Arenas).

entailed a loss of active lithium ions and the increase of the anodic resistance due to the growth of a film (Solid Electrolyte Interface or *SEI*). More recently, Christensen and Newman developed a model based on the chemistry of the *SEI* (e.g. film properties) and the different transport phenomena involved during its formation [6]. Although this model describes the film-growth characteristics, its application is limited, because it does not account for other coupled phenomena occurring across the cell. This limitation is likely due to the complexity of the film formation and the computational efforts demanded to solve the entire problem.

Temperature effects on the performance and safety of the batteries are critical, especially in automotive applications where battery packaging and environmental conditions may lead to extreme temperatures. However, unlike capacity fade, thermal effects are subjected to more inputs (e.g. heat generation due to reactions, entropy changes, Joule heating) during cycling. Different thermal models considering cell geometry and battery stacks have been proposed in literature for the Li-ion system [7,8]. However, none of them has considered the coupling between the thermal effects and capacity fade effect occurring at anode and cathode. Thus, one of the objectives of this work is to analyze, through a model development, the interactions arising due to the coupling of thermal and degradation phenomena during cycle life tests. The model presented in this work is originally based on the model validated with experimental data conducted by Doyle et al. [9], the thermal effects reported by Gu and Wang [7] and Cai and White [8], the capacity fade effects due to an electrochemical reduction at anode by Ning et al. [5], and the dissolution of  $\text{Li}_y\text{Mn}_2\text{O}_4$  particles in the cathode side by Park et al. [10]. Comparisons between simple and complex models are carried out to analyze individual degradation effects during cycle life tests considering thermal balances. Some modifications are proposed in the model to better represent the behavior of the cell and accelerate the convergence of the model. A forthcoming work will be focused on determining the phenomena sensitivity, the accuracy of the kinetics parameters of the model and validating the model with the experimental performance of the cell.

## 2. Modeling

The dual-lithium insertion cell modeled in this work is composed of a negative electrode current collector, negative electrode ( $\text{Li}_x\text{C}_6$ ), separator, positive electrode ( $\text{Li}_y\text{Mn}_2\text{O}_4$ ) and positive electrode current collector as shown in Fig. 1. The electrolyte is a solution of  $\text{LiPF}_6$  in a nonaqueous liquid mixture of ethylene carbonate (EC) and dimethyl carbonate (DMC) [9]. The schematic in Fig. 1 also shows the dimensions of the cross-section of the cell modeled in this study with a 1-D domain. The intercalation and deintercalation reactions taking place at the electrode/electrolyte interface can be written as:



During discharge, lithium ions insert into solid particles at the cathode, and de-insert from particles at the anode. The opposite occurs during the charging processes. The diffusive process in the solid phase and the electrolyte is fundamental in the mechanisms of discharge and charge of the cell, as well as the heat generation and heat transfer across the cell. The governing equations for the mathematical model presented in this work, as well as the initial

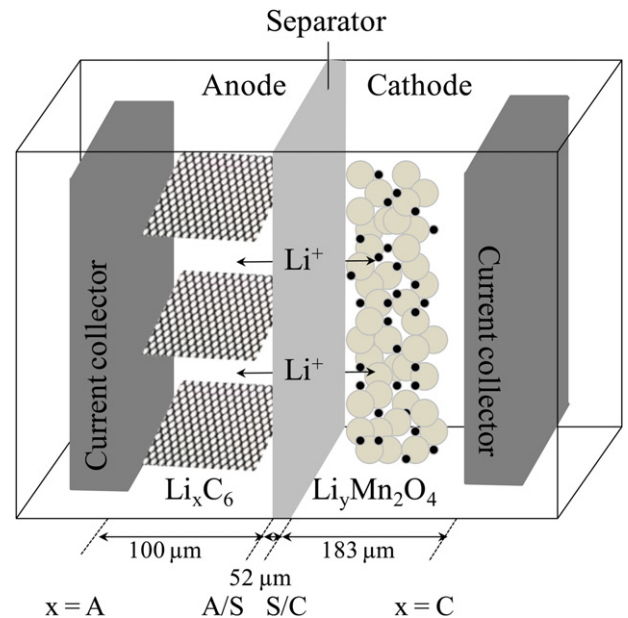


**Fig. 1.** Schematic of the dual Li-ion cell showing the cross-section (*x*-axis) modeled in this work (not scaled). The cell consists of a negative electrode current collector, negative electrode ( $\text{Li}_x\text{C}_6$ ), separator, positive electrode ( $\text{Li}_y\text{Mn}_2\text{O}_4$ ) and positive electrode current collector. The electrolyte is a solution of  $\text{LiPF}_6$  in a nonaqueous liquid mixture of ethylene carbonate and dimethyl carbonate.

and boundary conditions required to solve the equations are shown in Table 1. The mathematical model describes the diffusion (e.g. porous electrode theory) and conduction of Li ions with conservation of charge (e.g. Ohm's law) in the solid and electrolyte phases across the cell, e.g. anode, separator and cathode. Further details of the material and charge balances have been described elsewhere [9]. The model also incorporates energy balances to describe the thermal distributions across the cell [7,8], the equations to describe capacity fade effects due to the loss of active lithium ions by electrochemical reduction [5] and volume changes due to the dissolution of  $\text{Li}_y\text{Mn}_2\text{O}_4$  particles at the cathode side [10]. Note that a modification was applied to the model to transform the discrete expressions reported in Ref. [5] for the lithium concentration in the anode and resistance of *SEI* formation into derivative terms. These changes remarkably improved the convergence of the model. Table 2 details the parameters and formulas used in the lithium-ion battery model reported in Table 1.

Numerical simulations were run in order to solve the model reported in Table 1. Matlab™ 2010b and COMSOL™ MULTIPHYSICS 4.1 were used together for this purpose. Second-order Lagrange quadratic polynomials were used as shape functions, along with an interactive-smart mesh used to discretize the domain using the Finite Element Method. An Intel Core i7 central processing unit running at 3.47 GHz with a random access memory of 8.00 GB was used to carry out the calculations.

## 3. Results

The first set of simulations performed to test our model were comparisons of potential vs. capacity of the cell at different discharge rates (plots not shown). These computations were run under the conditions reported by Doyle et al. (refer to Fig. 4 in Ref. [9]). Our simulations showed that the model was capable of describing the experimental plots shown by Doyle et al., and only slight deviations were observed likely related with the choice of the numerical method used to solve the model. For example, Doyle

**Table 1**

Governing equations, initial and boundary conditions comprising the lithium-ion battery model.

Region of the cell	Balance	Governing equations	Boundary or initial condition
Anode	Material, solid phase	$\frac{\partial c_{s,n}}{\partial t} = D_{s,n} \frac{1}{r^2} \frac{\partial}{\partial r} \left( r^2 \frac{\partial c_{s,n}}{\partial r} \right)$	$c_{s,n} _{t=0} = c_{n,ini}$
	Charge, solid phase	$\sigma_{eff,n} \frac{\partial^2 \Phi_{1,n}}{\partial x^2} = a_n F j_n$	$-D_{s,n} \frac{\partial c_{s,n}}{\partial r} _{r=0} = 0 \quad -D_{s,n} \frac{\partial c_{s,n}}{\partial r} _{r=R_p,n} = j_n$
	Charge, liquid phase	$-\frac{\partial}{\partial x} \left( \kappa_{eff,n} \frac{\partial \Phi_{2,n}}{\partial x} \right) + \frac{2RT(1-t_+^0)}{F} \frac{\partial}{\partial x} \left( \kappa_{eff,n} \frac{\partial \ln c}{\partial x} \right) = a_n F j_n$	$\Phi_{1,n} _{x=A} = 0 \quad -\sigma_{eff,n} \frac{\partial \Phi_{1,n}}{\partial x} _{x=A/S} = 0$
	Material, liquid phase	$\varepsilon_{e,n} \frac{\partial c}{\partial t} = \frac{\partial}{\partial x} \left( D_{eff,n} \frac{\partial c}{\partial x} \right) + (1-t_+^0) a_n j_n$	$-\kappa_{eff,n} \frac{\partial \Phi_{2,n}}{\partial x} _{x=A} = 0 \quad -\kappa_{eff,n} \frac{\partial \Phi_{2,n}}{\partial x} _{x=A/S} = -\kappa_{eff,s} \frac{\partial \Phi_{2,s}}{\partial x} _{x=A/S}$
	Energy	$\rho_n C_p \frac{\partial T}{\partial t} = \frac{\partial}{\partial x} \left( \lambda_n \frac{\partial T}{\partial x} \right) + \left( \Phi_{1,n} - \Phi_{2,n} - U_n + T \frac{\partial U_n}{\partial T} \right) a_n F j_n + \sigma_{eff,n} \left( \frac{\partial \Phi_{1,n}}{\partial x} \right)^2 + \kappa_{eff,n} \left( \frac{\partial \Phi_{2,n}}{\partial x} \right)^2 + \frac{2RT(1-t_+^0)}{F} \kappa_{eff,n} \frac{\partial \ln c}{\partial x} \frac{\partial \Phi_{2,n}}{\partial x}$	$c _{t=0} = c_0 \quad -D_{eff,n} \frac{\partial c}{\partial x} _{x=A} = 0 \quad -D_{eff,n} \frac{\partial c}{\partial x} _{x=A/S} = -D_{eff,s} \frac{\partial c}{\partial x} _{x=A/S}$ $T_n _{t=0} = T_{env} \quad -\lambda_n \frac{\partial T}{\partial x} _{x=A} = h(T - T_{env})$ $-\lambda_n \frac{\partial T}{\partial x} _{x=A/S} = -\lambda_s \frac{\partial T}{\partial x} _{x=A/S}$
Separator	Charge, liquid phase	$-\kappa_{eff,s} \frac{\partial \Phi_{2,s}}{\partial x} + \frac{2RT(1-t_+^0)}{F} \kappa_{eff,s} \frac{\partial \ln c}{\partial x} = 0$	$-\kappa_{eff,n} \frac{\partial \Phi_{2,n}}{\partial x} _{x=A/S} = -\kappa_{eff,s} \frac{\partial \Phi_{2,s}}{\partial x} _{x=A/S}$
	Material, liquid phase	$\varepsilon \frac{\partial c}{\partial t} = \frac{\partial}{\partial x} \left( D_{eff,s} \frac{\partial c}{\partial x} \right)$	$-\kappa_{eff,s} \frac{\partial \Phi_{2,s}}{\partial x} _{x=S/C} = -\kappa_{eff,p} \frac{\partial \Phi_{2,p}}{\partial x} _{x=S/C}$
	Energy	$\rho_s C_p \frac{\partial T}{\partial t} = \frac{\partial}{\partial x} \left( \lambda_s \frac{\partial T}{\partial x} \right) + \kappa_{eff,s} \left( \frac{\partial \Phi_{2,s}}{\partial x} \right)^2 + \frac{2RT(1-t_+^0)}{F} \kappa_{eff,s} \frac{\partial \ln c}{\partial x} \frac{\partial \Phi_{2,s}}{\partial x}$	$c _{t=0} = c_0 \quad -D_{eff,n} \frac{\partial c}{\partial x} _{x=A/S} = -D_{eff,s} \frac{\partial c}{\partial x} _{x=A/S}$ $-D_{eff,s} \frac{\partial c}{\partial x} _{x=S/C} = -D_{eff,p} \frac{\partial c}{\partial x} _{x=S/C}$ $T_s _{t=0} = T_{env} \quad -\lambda_n \frac{\partial T}{\partial x} _{x=A/S} = -\lambda_s \frac{\partial T}{\partial x} _{x=A/S}$ $-\lambda_s \frac{\partial T}{\partial x} _{x=S/C} = -\lambda_p \frac{\partial T}{\partial x} _{x=S/C}$
Cathode	Material, solid phase	$\frac{\partial c_{s,p}}{\partial t} = D_{s,p} \frac{1}{r^2} \frac{\partial}{\partial r} \left( r^2 \frac{\partial c_{s,p}}{\partial r} \right)$	$c_{s,p} _{t=0} = c_{p,ini}$
	Charge, solid phase	$\sigma_{eff,p} \frac{\partial^2 \Phi_{1,p}}{\partial x^2} = a_p F j_p$	$-D_{s,p} \frac{\partial c_{s,p}}{\partial r} _{r=0} = 0 \quad -D_{s,p} \frac{\partial c_{s,p}}{\partial r} _{r=R_p,p} = j_p$
	Charge, liquid phase	$-\frac{\partial}{\partial x} \left( \kappa_{eff,p} \frac{\partial \Phi_{2,p}}{\partial x} \right) + \frac{2RT(1-t_+^0)}{F} \frac{\partial}{\partial x} \left( \kappa_{eff,p} \frac{\partial \ln c}{\partial x} \right) = a_p F j_p$	$-\sigma_{eff,p} \frac{\partial \Phi_{1,p}}{\partial x} _{x=S/C} = 0 \quad -\sigma_{eff,p} \frac{\partial \Phi_{1,p}}{\partial x} _{x=C} = I_{ap}$
	Material, liquid phase	$\varepsilon_{e,p} \frac{\partial c}{\partial t} = \frac{\partial}{\partial x} \left( D_{eff,p} \frac{\partial c}{\partial x} \right) + (1-t_+^0) a_p j_p$	$\Phi_{1,p} _{x=C} = E_{cell}$
	Energy	$\rho_p C_p \frac{\partial T}{\partial t} = \frac{\partial}{\partial x} \left( \lambda_p \frac{\partial T}{\partial x} \right) + \left( \Phi_{1,p} - \Phi_{2,p} - U_p + T \frac{\partial U_p}{\partial T} \right) a_p F j_p + \sigma_{eff,p} \left( \frac{\partial \Phi_{1,p}}{\partial x} \right)^2 + \kappa_{eff,p} \left( \frac{\partial \Phi_{2,p}}{\partial x} \right)^2 + \frac{2RT(1-t_+^0)}{F} \kappa_{eff,p} \frac{\partial \ln c}{\partial x} \frac{\partial \Phi_{2,p}}{\partial x}$	$-\kappa_{eff,p} \frac{\partial \Phi_{2,p}}{\partial x} _{x=C} = 0 \quad -\kappa_{eff,s} \frac{\partial \Phi_{2,s}}{\partial x} _{x=S/C} = -\kappa_{eff,p} \frac{\partial \Phi_{2,p}}{\partial x} _{x=S/C}$ $c _{t=0} = c_0 \quad -D_{eff,p} \frac{\partial c}{\partial x} _{x=C} = -D_{eff,s} \frac{\partial c}{\partial x} _{x=S/C}$ $T_p _{t=0} = T_{env} \quad -\lambda_s \frac{\partial T}{\partial x} _{x=S/C} = -\lambda_p \frac{\partial T}{\partial x} _{x=S/C}$ $-\lambda_p \frac{\partial T}{\partial x} _{x=C} = h(T_{env} - T)$

**Table 2**

Properties, parameters and formulas used in the lithium-ion battery model [5–10].

Description	Anode	Separator	Cathode
Initial electrolyte salt concentration		$c_0 = 2000 \text{ mol m}^{-3}$	
Maximum concentration in intercalation material	$c_n^t = 26,390 \text{ mol m}^{-3}$		$c_p^t = 22,860 \text{ mol m}^{-3}$
Initial concentration of Li <sup>+</sup> in solid phase	$c_{s,n}^0 = 14,870 \text{ mol m}^{-3}$		$c_{s,p}^0 = 3900 \text{ mol m}^{-3}$
State of charge	$SOC_n = \frac{c_{s,n}}{c_n^t}$		$SOC_p = \frac{c_{s,p}}{c_p^t}$
Solid phase Li-diffusivity in the particles	$D_{s,n} = 3.9 \times 10^{-14} \text{ m}^2 \text{ s}^{-1}$		
Volume fraction of electrolyte phase	$\varepsilon_{e,n} = 0.357$		$D_{s,p} = 1 \times 10^{-13} \text{ m}^2 \text{ s}^{-1}$
Volume fraction of polymer phase	$\varepsilon_{p,n} = 0.146$		$\varepsilon_{e,p} = 0.444$
Volume fraction of conductive filler	$\varepsilon_{f,n} = 0.026$		$\varepsilon_{p,p} = 0.186$
Separator porosity		$\varepsilon = 1$	$\varepsilon_{f,p} = 0.073$
Specific surface area	$a_n = \frac{3\varepsilon_{s,n}}{r_{p,n}} = \frac{3(1 - \varepsilon_{e,n} - \varepsilon_{p,n} - \varepsilon_{f,n})}{r_{p,n}}$ $= 1.1304 \times 10^5 \text{ m}^2$		$a_p = \frac{3\varepsilon_{s,p}}{r_{p,p}} = 1.11375 \times 10^5 \text{ m}^2$
Salt diffusivity in the electrolyte		$D_e = 10^{-4.43 - \frac{54}{T-229-5 \cdot 10^{-3}c} - 0.22 \times 10^{-3}c}$ $\times 10^{-4} \text{ m}^2 \text{ s}^{-1}$	
Effective salt diffusivity in the electrolyte		$D_{eff} = D_{e,n} \varepsilon_e^{1.5} \text{ m}^2 \text{ s}^{-1}$	
Electronic conductivity of the solid phase	$\sigma_{0,n} = 100 \text{ S m}^{-1}$		$\sigma_{0,p} = 3.8 \text{ S m}^{-1}$
Effective conductivity of the solid phase	$\sigma_{eff,n} = \sigma_{0,n}(1 - \varepsilon_{e,n} - \varepsilon_{p,n} - \varepsilon_{f,n})^{1.5}$		$\sigma_{eff,p} = \sigma_{0,p} \varepsilon_s^{1.5}$
Ionic conductivity of the electrolyte	$\kappa_e = (-10.5c + 0.668 \times 10^{-3}c^2 + 0.494 \times 10^{-6}c^3 + 0.074cT - 1.78 \times 10^{-5}c^2T - 8.86 \times 10^{-10}c^3T - 6.96 \times 10^{-5}cT^2 + 2.80 \times 10^{-8}c^2T^2)^2 \times 10^{-4} \text{ S m}^{-1}$		
Effective ionic conductivity	$k_{eff,s} = \kappa_e \varepsilon_s$		
Intercalation/Deintercalation rate constant	$k_n = 2 \times 10^{-6} \text{ mol}^{-0.5} \text{ s}^{-1}$		$k_{eff,p} = k_e \varepsilon_p$
Intercalation/Deintercalation current density	$j_n^{int/dein} = k_n(c_n^t - c_{s,n} _{r=R_p,n})^{0.5} (c_{s,n} _{r=R_p,n})^{0.5}$ $c^{0.5} \left( \exp \left( \frac{0.5F}{RT} \eta_n \right) - \exp \left( -\frac{0.5F}{RT} \eta_n \right) \right)$		$k_p = 2 \times 10^{-6} \text{ mol}^{-0.5} \text{ s}^{-1}$ $j_p^{int/dein} = k_p(c_p^t - c_{s,p} _{r=R_p,p})^{0.5} (c_{s,p} _{r=R_p,p})^{0.5} c^{0.5} \left( \exp \left( \frac{0.5F}{RT} \eta_p \right) - \exp \left( -\frac{0.5F}{RT} \eta_p \right) \right)$
Overpotential	$\eta_n = \Phi_{1,n} - \Phi_{2,n} - U_n - (j_n^{int/dein} + j_{SEI}) R_{SEI}$		$\eta_p = \Phi_{1,p} - \Phi_{2,p} - U_p$
Open circuit potential	$U_n = U_{n,ref} + (T - T_{ref}) \left( \frac{\partial U_n}{\partial T} \right)_n$		$U_p = U_{p,ref} + (T - T_{ref}) \left( \frac{\partial U_p}{\partial T} \right)_p$
Open circuit potential at a reference temperature	$U_{n,ref} = -0.16 + 1.32 \exp(-3SOC_n) + 10 \exp(-2000SOC_n)$		$U_{p,ref} = 4.19829 + 0.0565661 \tanh(8.60942 - 14.5546SOC_p)$ $-0.0275479 \left( \frac{-1.90111}{1 + \frac{1}{(0.998432 - SOC_p)^{0.492465}}} \right)$ $-0.157123 \exp(-0.04738SOC_p^8)$ $+0.810239 \exp(-40[-0.133875 + SOC_p])$
Current density of SEI formation	$j_{SEI} = -j_{SEI}^0 \exp \left( \frac{0.5F}{RT} \eta_{SEI} \right) \quad \text{If } I_{ap} < 0$		
Exchange current density of SEI formation	$j_{SEI}^0 = 0.8 \times 10^{-7} \text{ A m}^{-2}$		
Resistance of SEI formation	$\frac{\partial R_{SEI}}{\partial t} = \frac{j_{SEI} M_{SEI}}{\rho_{SEI} F k_{SEI}}$		
Equilibrium Potential of SEI formation	$U_{SEI} = 0.38 \text{ V}$		
Molecular weight	$M_{SEI} = 0.1 \text{ kg mol}^{-1}$		
Density of SEI film	$\rho_{SEI} = 2.1 \times 10^3 \text{ g m}^{-3}$		
Conductivity of SEI film	$\kappa_{SEI} = 3.79 \times 10^{-7} \text{ S m}^{-1}$		
Reference rate constant of particle dissolution			$k_0 = 3.41 \times 10^5 \text{ s}^{-1}$

(continued on next page)

et al. used Finite Differences instead of Finite Element Method. The intention of this work is to analyze the degradation and the interactions arising due to the coupling of capacity fade and thermal effects over the life of a cell. Therefore, the next step was to cycle the battery using the typical cycling profile shown in Fig. 2. A baseline model (i.e. without coupled effects) was compared with more comprehensive ones to analyze systematically in the effects of the following three combined factors on cell performance: 1) thermal balance, 2) thermal balance + capacity fade at the anode, and 3) thermal balance + capacity fade at the cathode.

### 3.1. Current density profile

Fig. 2 shows the current density profile (i.e. single cycle) for the charge-depleting cycle life test reported by the Idaho National Laboratory in the battery test manual for plug-in hybrid electric vehicles [11]. This waveform is intended to allow the vehicle to operate in hybrid and electric modes with a net decrease in the battery state of charge (SOC) and with an observable degradation of the battery from cycle to cycle. Thus, this typical cycle fulfills the requirements to test the model that has been developed in this work. This profile was used to run all the simulations reported in this work. Note that for batteries, this profile assumes that the degradation rate is a function of the high current densities passing through each cell. Then, the current passing through each cell will be proportional to the total cell cross-sectional area (which will depend on how the cell is engineered), and the number of cells in parallel. Therefore, for this study it is recognized that the degradation effects over cycling (e.g. capacity higher than 50 C). In future work, the sensitivity of this rate and the current passing through each cell will be explored in more details.

### 3.2. Thermal contributions without capacity fade effects

The first cycling tests using the profile in Fig. 2 were computed to analyze the thermal effects on the behavior of the battery cell. For this phase of the work different heat transfer coefficients ( $h$ ) as well as isothermal and adiabatic conditions were used in the model. These results are shown in Fig. 3 for 50 cycles (equivalent to 18,050 s on cell operation). No capacity fade effects were considered at this stage of the modeling and the linear dependence of the OCP is neglected,  $\partial U_n / \partial T = 0$  [7]. As shown in Fig. 3, the highest temperatures are reached when the cell is placed under adiabatic

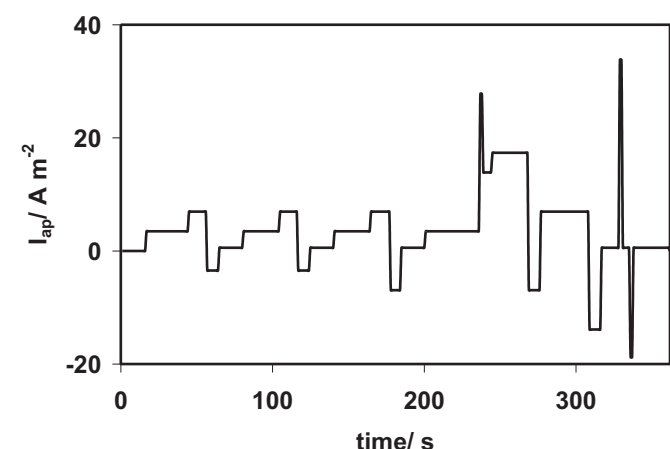


**Fig. 2.** Current density profile for the charge-depleting cycle life test (i.e. a single cycle) [11].

**Table 2** (continued)

Description	Anode	Separator	Cathode
Activation energy of particle dissolution			
Arrhenius equation for particle dissolution			
Particle dissolution rate			
Volume fraction of cathode active material			
Thermal conductivity			
Density			
Specific heat			
Convective heat transfer coefficient			
	$\lambda_n = 5 \text{ W m}^{-1} \text{ K}^{-1}$		
	$\rho_n = 2500 \text{ mol m}^{-3}$		
			$E_a = 72.840 \text{ J mol}^{-1}$
			$k_{diss} = k_0 \exp\left(\frac{-E_a}{RT}\right)$
			$X_a = 1 - (1 - k_{diss})^3$
			$\varepsilon_{sp} = (1 - \varepsilon_{en} - \varepsilon_{pn} - \varepsilon_{jn}) \left(1 - 0.152 \frac{X_a}{1 + X_a}\right)$
			$\lambda_p = 5 \text{ W m}^{-1} \text{ K}^{-1}$
			$\rho_p = 1500 \text{ mol m}^{-3}$
			$\lambda_s = 1 \text{ W m}^{-1} \text{ K}^{-1}$
			$\rho_s = 1200 \text{ mol m}^{-3}$
			$C_p = 700 \text{ J g}^{-1} \text{ K}^{-1}$
			$h = 1 \text{ W m}^{-2} \text{ K}^{-1}$

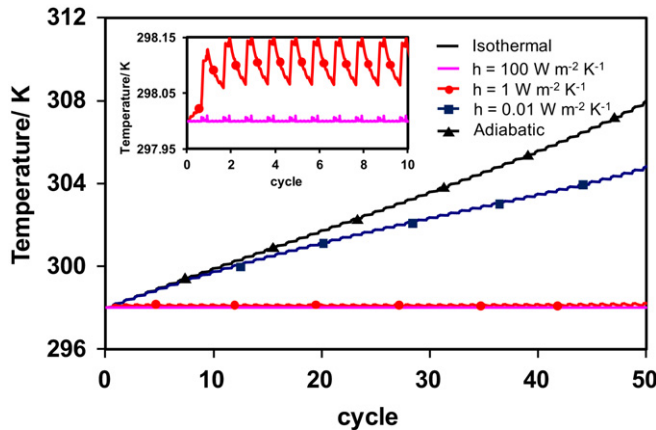


**Fig. 3.** Computed temperature profiles at the interface formed between the cathode and the current collector at different heat transfer coefficients labeled on the figure.

conditions, followed by when the process is performed under the lowest heat transfer coefficient,  $h = 0.01 \text{ W m}^{-2} \text{ K}^{-1}$ . These effects are not surprising since the cell lies under isolated conditions and low heat exchange with the environment, respectively in each one of these simulation runs. On the other hand, when the cell exchanges heat easily with the environment ( $h \geq 1 \text{ W m}^{-2} \text{ K}^{-1}$ ), it attains a steady temperature profile over cycling since there is not sufficient heat generated to cause a rise in the temperature. Typically  $h$  is assumed to be  $1 \text{ W m}^{-2} \text{ K}^{-1}$  but there is expected to be a wide variation in this value depending on how the cell is manufactured. Two regions are of interest under these conditions. In the first region, during the first 236 s of each cycle (low current zone in Fig. 2), the heat produced in the cell is mostly exchanged with the surroundings. The opposite behavior occurs in the second region (~last 236–268 s of each cycle) when larger discharge/charge current densities are imposed on the cell, producing enough heat to increase the temperature within the cell. This observation is repeated through each cycle and a steady temperature profile is maintained. The rises and drops in temperature shown in the inset of Fig. 3 correspond to abrupt and intermediate-low  $\text{Li}^+$  intercalation/deintercalation processes, respectively (plots not shown). It is worth highlighting that steeper slopes are attained in the temperature profiles when higher currents are applied to the cell. Apparently, these effects would multiply when battery stacks are cycled over the long term, whence thermal overheating would be also produced. It is worth mentioning that these simulations do yet to account for effects that may be observed near the current collectors where higher localized current densities may be observed (e.g. Joule heating effect). The variation of the temperature across the cell was found to be insignificant regardless of the condition utilized in the cell. This behavior could be associated with the fact that the present model considers only the cross-section of the cell. Larger effects might be expected along the height of the cell where Joule heating effects may become important [7].

### 3.3. Capacity fade effects due to anode SEI formation

In Fig. 4 anode degradation is assumed from SEI formation, and it is assumed that the SEI continues to increase with each cycle. As such, Fig. 4 shows the computed potential profiles at different exchange current densities of the electrolyte reduction reaction occurring during the charge process at the anode (i.e. different rates for SEI formation). This reaction is used to account for the capacity fade effects in the battery due to the growth of the SEI [5].

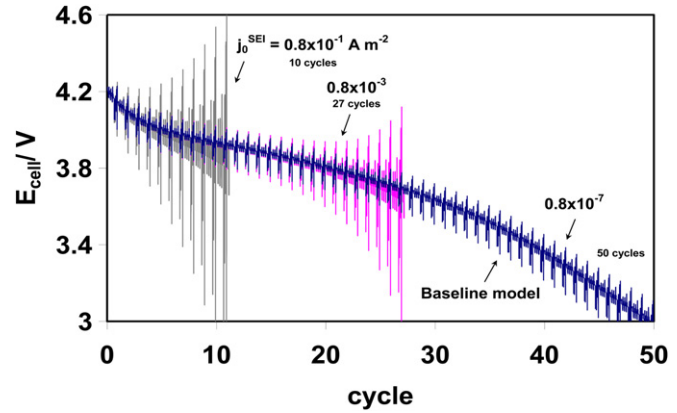


**Fig. 4.** Computed cell potential for analyzing the capacity fade at anode assuming a continuous formation of SEI film throughout the cell life. Different exchange current densities accounting for SEI formation are evaluated using a heat transfer coefficient set to  $1 \text{ W m}^{-2} \text{ K}^{-1}$ . Cycles 0–50.

Thermal effects are also included in this model. As observed from these plots, the  $E_{cell}$  oscillates at the two highest  $j_{SEI}^0$  values ( $0.08$  and  $0.0008 \text{ A m}^{-2}$ ), probably due to the significant increase of the reduction rate for this reaction as the number of cycles are increasing ( $j_{SEI}$ ). This process causes a loss of active lithium and an increase of impedance ( $R_{SEI}$ ) at the anode (plots not shown), as well as the oscillation of the charge in the solid phase (refer to  $\Phi_1$  in Table 1) and a minor oscillation of the electric potential in the liquid phase ( $\Phi_2$ ). On the other hand, when the capacity fade is not considered in the model (i.e. baseline model) or low contributions of the reduction reaction are considered ( $j_{SEI}^0 = 0.8 \times 10^{-7} \text{ A m}^{-2}$ ), the  $E_{cell}$  profiles resemble those obtained experimentally (plots not shown).  $\Phi_1$  and  $\Phi_2$  do not oscillate for these former cases. However, the simulations carried out with the baseline model, using  $j_{SEI}^0 = 0.8 \times 10^{-7}$  or  $0.8 \times 10^{-5} \text{ A m}^{-2}$  (not shown) produce virtually the same  $E_{cell}$  profiles. This behavior is associated with the low  $j_{SEI}^0$  values used in the simulations, which are not sufficient to generate an important input of the SEI formation. As previously described, larger  $j_{SEI}^0$  values lead to the oscillation of  $E_{cell}$ , which would not represent a realistic description of the behavior of the cell. This phenomenon suggests that the formation of the SEI at the anode would entail a different action. Perhaps, its formation might start occurring during the early cycles of the test, and reach a steady-state for the consecutive cycles. In fact, during the manufacturing of Li-ion batteries, they are initially cycled for some cycles to form a pseudo-steady-state SEI, and thus avoiding the loss of  $\text{Li}^+$  ions from the electrolyte during subsequent operation. Under the scheme in Fig. 4, a steady loss of active lithium and impedance growth would be also implied in the model. In fact, important phenomena associated with the SEI formation are apparent from literature [4]. Numerous reactions could be involved in the SEI formation when the anode contacts an oxidant (e.g. solvent, air) [6], whence the film composition has been difficult to determine [2]. Nevertheless, it is known that the film is to some extent electronically insulating whereby continuous solvent and salt reduction at the SEI/solution interface is hindered [6]. Thus, stable films form on graphite electrodes during the first two cycles [12] and any further change of their structure occurs only under abusive conditions or long storage [2]. Solvent molecules are impeded from arriving at the anode, whereas  $\text{Li}^+$  ions are transferred across the film as vacancies or interstitials [6]. Accordingly, the formation of a steady film after the first two cycles is used below to describe the capacity fade effects during cycle life tests.

**Fig. 5** shows  $I_{ap}$  (profile in **Fig. 2**) and  $E_{cell}$  profiles for cycles 49–50 assuming that the SEI thickness and consequently the impedance growth remain unchanged after the first two cycles according to information provided in the literature [2,4,13]. It is acknowledged that for some particular anodes, the SEI continues growing but its effects of the addition growth after the initial SEI formation can be considered negligible [14], unless it overcomes a major damage which require a big loss of  $\text{Li}^+$  ions to repair it. Instead of the discharge/charge capacity plots,  $E_{cell}$  profiles are presented since cycles containing different waveforms were applied in this study. The curves in **Fig. 5** were overstated by the use of large values of  $j_{SEI}^0$  to appreciate the effects of capacity fade. However, none of them present an oscillatory behavior as those shown in **Fig. 4**. The difference is evident between the model that does not consider a capacity fade input and the one that accounts for this effect. Note that the baseline model produces virtually similar results with the simulations carried out at  $j_{SEI}^0 = 0.8 \times 10^{-7} \text{ A m}^{-2}$ , which is likely associated with a low input of this exchange current density. As observed in the discharge regions of the  $I_{ap}$  profile, the  $E_{cell}$  is in general lower for  $j_{SEI}^0 = 0.8 \times 10^{-1} \text{ A m}^{-2}$ , following this trend the value of  $0.8 \times 10^{-3} \text{ A m}^{-2}$ . This suggests that higher  $j_{SEI}^0$  values accelerate the SEI precipitation, whereby the film resistance presented to lithiate/delithiate  $\text{Li}^+$  ions increases during the first two cycles. Under this context, larger  $j_{SEI}^0$  values would cause a bigger capacity fade of the cell. Likewise, **Fig. 5** clearly shows the prediction of the accelerated degradation imposed to the cell over cycling. Thus, since oscillatory behaviors are obtained for the  $E_{cell}$  when the SEI resistance is allowed to grow (refer to **Fig. 4**), the impedance of the film should remain steady during most of the cycling.

### 3.4. Capacity fade effects due to changes in the volume fraction of the cathode

Considering cathode degradation, **Fig. 6** shows two different energy activation ( $E_a$ ) values describing the volume change due to dissolution of the  $\text{Li}_y\text{Mn}_2\text{O}_4$  particles at the cathode. The value of  $72,840 \text{ J mol}^{-1}$  reported for this process was selected from Ref. [10], and it was only decreased by an order of magnitude to sensitize its contribution. **Fig. 6a** shows a clear difference in  $E_{cell}$  values when two different  $E_a$  values are used in the simulations during the first five cycles. Not surprisingly, lower  $E_{cell}$  values are obtained when the energy activation to dissolve  $\text{Li}_y\text{Mn}_2\text{O}_4$  particles is lower, indicating that the cell capacity degrades faster when the energetic

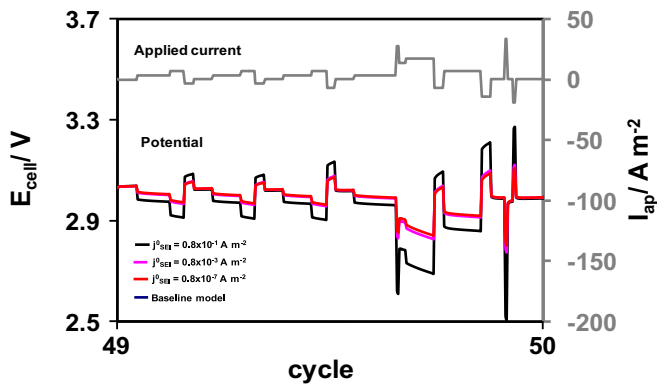


**Fig. 5.** Computed cell potential for analyzing the capacity fade at anode assuming the formation of SEI film only occurs during the first two cycles and then remains constant. Different exchange current densities accounting for SEI formation are evaluated using a heat transfer coefficient set to  $1 \text{ W m}^{-2} \text{ K}^{-1}$ . Simulations of the baseline model and  $j_{SEI}^0 = 0.8 \times 10^{-7} \text{ A m}^{-2}$  produce the same result. Cycles 49–50.

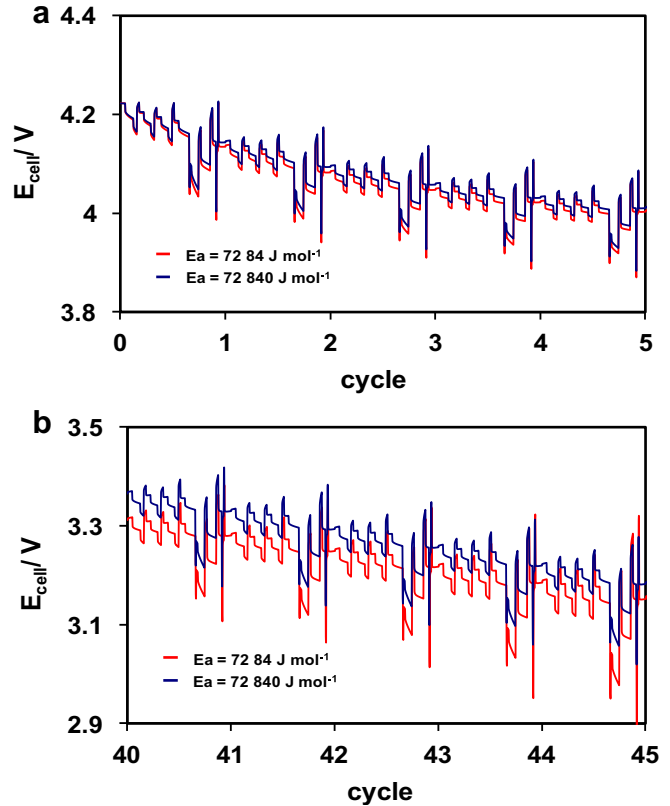


**Fig. 6.** Computed cell potential for analyzing the capacity fade at cathode assuming a change in volume fraction of this electrode due to the dissolution of the  $\text{Li}_y\text{Mn}_2\text{O}_4$  particles. Two different energy activation values are evaluated using a heat transfer coefficient set to  $h = 1 \text{ W m}^{-2} \text{ K}^{-1}$ . Capacity fade at anode is disregarded. Cycles 1–5 and 40–45 are shown in (a) and (b), respectively.

barrier to perform this reaction is decreased. A comparison of the  $E_{cell}$  profiles given for cycles 1–5 (**Fig. 6a**) and 40–45 (**Fig. 6b**) shows that a larger difference between the two  $E_a$  values is observed as the cycling of the cell becomes longer, whereby the degradation of the cell progressively increases with cycling. Variations in the standard rate constant of the dissolution of  $\text{Li}_y\text{Mn}_2\text{O}_4$  particles ( $k_0$ ) did not produce differences in the computed  $E_{cell}$ . This might be due to the fact that  $k_0$  and  $E_a$  are statistically correlated in the  $k_{diss}$  expression (refer to **Table 2**), and  $k_0$  is not sensitive to the model under the

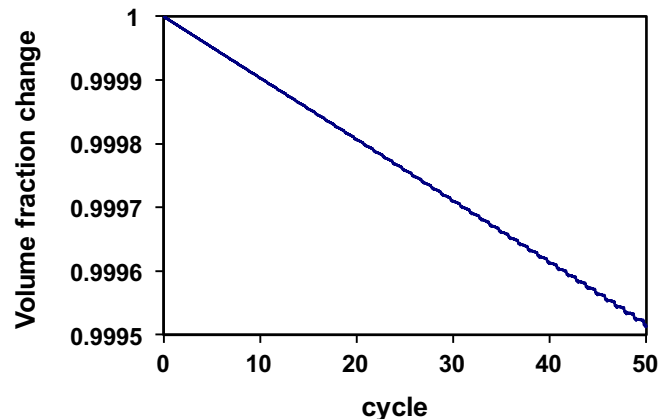


**Fig. 7.** Computed volume fraction ( $V/V_{mi}$ ) occurring in the cathode due to the dissolution of the  $\text{Li}_y\text{Mn}_2\text{O}_4$  particles. An energy activation value of  $72,840 \text{ J mol}^{-1}$  and a heat transfer coefficient of  $h = 1 \text{ W m}^{-2} \text{ K}^{-1}$  were utilized in the calculations.

analyzed conditions. The results obtained for this specific degradation mode need to be experimentally validated in order to determine the contributions of the dissolution of the  $\text{Li}_y\text{Mn}_2\text{O}_4$  particles operating in real Li-ion batteries (e.g. any potential correlation involving heat generation). Presumably, other important factor that should be analyzed is the migration and subsequently deposition of  $\text{Mn}^{2+}$  ions in the anode, which could also lead to the capacity fade of the battery.

Fig. 7 shows the volume fraction ( $V/V_{ini}$ ) changes occurring in the cathode due to the dissolution of the  $\text{Li}_y\text{Mn}_2\text{O}_4$  particles when an energy activation value of  $72,840 \text{ J mol}^{-1}$  is considered in the simulations. As observed in this plot, the volume fraction slightly augments linearly as cycling progresses. This behavior shows a similar trend described in the literature to a battery that is stored at  $20^\circ\text{C}$  for seven days, and larger volume fraction changes are observed when the battery is stored at  $50^\circ\text{C}$  during the same time [10].

#### 4. Conclusions

A comprehensive model has been presented to analyze the interactions between thermal and capacity fade effects during cycling of Li-ion cells. Heat generation due to reactions, entropy changes and Joule heating are considered for the thermal effects, whereas the capacity fade effects are accounted for by the loss of active lithium ions through electrochemical reduction at the anode (*SEI* formation), and the volume change due to dissolution of  $\text{Li}_y\text{Mn}_2\text{O}_4$  particles at the cathode. Some modifications in the capacity fade terms were carried out in order to improve the convergence of the model and account for the behavior of the cell. The baseline model presented in this work (e.g. mass and charge balances) agreed with the behavior presented in other studies.

Thermal effects analysis revealed that the cell exchanged considerably heat for  $h \geq 1 \text{ W m}^{-2} \text{ K}^{-1}$ , attaining a stable temperature profile during cycling. On the other hand, adiabatic conditions imposed to the cell produced a progressive rise in temperature since isolated conditions prevailed in the system. This effect was promoted by the application of high currents in the cell. The thermal analysis showed the need to incorporate these effects in the modeling of Li-ion cells, in addition to the integration of the heat produced by different cells in a battery.

Computed potential ( $E_{cell}$ ) profiles were used to discriminate the capacity fade effects due to *SEI* formation. Oscillatory potential profiles were obtained when this reaction was considered transient, and the impedance of the film grew over cycling. Otherwise, the  $E_{cell}$  profiles resemble the behavior obtained experimentally when these inputs were considered transient during the first two cycles, and steady for the rest of the test. Results from the evaluation of the capacity fade at cathode showed that the degradation of the cell is more prominent by using a lower energy activation value used to account for the dissolution of  $\text{Li}_y\text{Mn}_2\text{O}_4$  particles. Since capacity fade effects at anode and cathode were found to be significant in the degradation of the cell under specific conditions. It is needed to compare the model predictions with experimental data modulated over different degradation rates to be able to elucidate the importance of these effects under those circumstances.

#### Acknowledgments

The authors are indebted to General Motors, Automotive Partnership Canada and the Natural Sciences and Engineering Research Council of Canada for their financial support to carry out this work.

#### References

- [1] G. Ning, B. Popov, J. Electrochem. Soc. 151 (2004) A1584.
- [2] P. Arora, R.E. White, M. Doyle, J. Electrochem. Soc. 145 (1998) 3647.
- [3] R. Spotnitz, J. Power Sources 113 (2003) 72.
- [4] J. Christensen, J. Newman, J. Electrochem. Soc. 150 (2003) A1416.
- [5] G. Ning, R.E. White, B.N. Popov, Electrochim. Acta 51 (2006) 2012.
- [6] J. Christensen, J. Newman, J. Electrochem. Soc. 151 (2004) A1977.
- [7] W.B. Gu, C.Y. Wang, in: S. Surampudi, R.A. Marsh, Z. Ogumi, J. Prakash (Eds.), PV 99-25, The Electrochemical Society Proceedings Series, Pennington, NJ, 2000, p. 748.
- [8] L. Cai, R.E. White, J. Power Sources 196 (2011) 5985.
- [9] M. Doyle, J. Newman, A.S. Gozdz, C.N. Schmutz, J.M. Tarascon, J. Electrochem. Soc. 143 (1996) 1890.
- [10] J. Park, J.H. Seo, G. Plett, W. Lu, A.M. Sastry, Electrochim. Solid-State Lett. 14 (2011) A14.
- [11] [http://www.inl.gov/Battery Test Manual for Plug-in Hybrid Electric Vehicles \(September 2010\).](http://www.inl.gov/Battery Test Manual for Plug-in Hybrid Electric Vehicles (September 2010).)
- [12] M. Wachtler, J.O. Besenhard, M. Winter, J. Power Sources 94 (2001) 189.
- [13] C. Yuqin, L. Hong, W. Lie, L. Tianhong, J. Power Sources 68 (1997) 187.
- [14] C.S. Wang, A.J. Appleby, F.E. Little, J. Electroanal. Chem. 497 (2001) 33.